A Versatile Light Field Microscopy Platform for Multi-purpose Dynamic Volumetric Bio-imaging

Yangyang Bai, Matt Jones, Lauro Sebastian Ojeda, Janielle Cuala, Lynne Cherchia, Kate L. White, Senta K. Georgia, Scott E. Fraser, Thai V. Truong

Abstract

Light field microscopy (LFM) uses a plen-optic detection technique that samples both lateral and angular information of light rays by inserting a Micro-Lens Array (MLA) in the optical light path. With computational image reconstruction methods, 3D volume can be captured in a single snapshot, providing unprecedented imaging speed and throughput for a variety of biological imaging applications. In recent years, Fourier light field microscopy (FLFM) has been developed to improve the reconstruction speed and overall image quality by placing the MLA at the Fourier plane, rendering a set of angular views of the volume directly on the camera. In this work, we provide an implementation of FLFM platform that enables easy switching between wide range of imaging scenarios, from cell biology to system-level biology. Specifically, we construct the FLFM system with a wide field microscope body. By taking advantage of the integrated automatic nose-piece that carries multiple objectives in the microscope body, we achieve different imaging performances for the FLFM system by simple switching between different primary objectives. Additionally, we also provide an open-sourced software package for designing the system parameters, processing the experimentally measured point-spread function (PSF), and 3D reconstruction. We validate our system with single-bead images and showcase recordings of protein dynamics in the cell, calcium dynamics in a mouse islet, and zebrafish brain neural activities.

I. INTRODUCTION

Biological processes inherently occur in three dimensions (3D), ranging from intra-cellular trafficking to whole brain neural network activity[1–3]. Observing these processes in their native 3D context is essential for gaining a comprehensive understanding of how living systems develop, and how they function in health and malfunction in disease[4–6]. Volumetric microscopy techniques have greatly advanced our understanding of dynamic biological systems in 3D, yet challenges remain in capturing fast changing biological events at the relevant spatial-temporal resolution and coverage. Conventional volumetric imaging systems, such as confocal microscopy or Light Sheet Microscopy (LSM), acquire 3D volumetric images by scanning, either point by point or plane by plane across the entire volume[7,8]. While this strategy renders high resolution images, it is inherently slow due to the sequential scanning nature. Light Field Microscopy (LFM), on the other hand, obtains 3D volume in a single 2D snapshot without scanning[9–12]. This is achieved by inserting a micro-lens array (MLA) in the detection light path, recording synchronously both the spatial and angular information of the 3D sample's light field onto the 2D camera. The 3D information is then reconstructed computationally in post-processing by solving the inverse problem with knowledge of the microscope optical train[13–15]. Because of the non-scanning nature, LFM has been demonstrated to reach a high volumetric imaging speed, reaching up to 100 Hz[16–18], and opening up dynamic 3D imaging applications that are otherwise beyond the reach of scanning imaging modalities.

Currently, published LFM platforms have mainly been designed to work well for only single imaging scenarios[19–23], where the focus is to maximize the imaging performance at a particular set of volume coverage and resolution. For example, particle tracking in cell biology was achieved in a setup with high imaging resolution (~0.5 um) and small depth of view (DOV) (~6 um)[19], whereas whole-brain neural imaging in zebrafish larvae was implemented in platforms with larger DOV (~250 um) but lower resolution (~2 um)[18,23,16,17,22]. (Here, the DOV refers to the axial depth extent of the imaged volume where useful resolvable information can be collected and reconstructed.) These aforementioned examples were implemented with a specific set of hardware, lacking the flexibility to accommodate multiple imaging scenarios with diverse imaging performance requirements. This limitation has hindered the widespread adoption of LFM in biomedical research labs that do not have expertise in optics, as well as prevented the development of the LFM modality into a viable commercial product.

In this work, we developed a versatile LFM platform that allows for diverse bio-imaging in a flexible and user-friendly manner. We were inspired by the commercial Wide Field Microscopy (WFM) design where bio-imaging at different scales can be achieved by simply choosing different microscope objectives housed in a rotating turret. Thus, we constructed our LFM based on a commercial WFM body, with an add-on LFM detection module connected to the standard camera port, and without any modification to the main microscope body (Fig. 1a 1, Supplementary Fig. 1). By taking advantage of the rotating turret, we reasoned that a wide range of bio-imaging scenarios could be met by simply switching to a different primary objective without changing other hardware components in the LFM module (Table 1). This strategy marries the versatility and ease-of-use of the inverted microscope, a workhorse in many biomedical research labs, to the unique 3D imaging capability of LFM. We selected an off-the-shelf commercially-available MLA to achieve near optimal performance for all the objectives of interest (Fig. 1b). From the user's perspective, our platform offers user-friendliness in several aspects. The sample is mounted in the same way as in an inverted WFM, and thus existing experimental workflows can be readily adopted for LFM imaging. For 3D reconstruction, we provide an open-sourced software package, along with a detailed, step-by-step procedure for acquiring and processing the experimentally measured point spread function (PSF) that is used in the reconstruction. To showcase the versatility of our LFM platform, we demonstrated its performance in three imaging scenarios that span a wide range of biologically relevant scales: observing protein dynamics in cultured cells, recording calcium signaling dynamic in an ex vivo mouse pancreatic islet, and characterizing whole-brain neuronal seizure in an intact zebrafish larva.

II. RESULT AND DISCUSSION

A. Overview of the versatile LFM platform

Our versatile LFM platform was constructed by adding a LFM module to the detection path of a commercial inverted WFM body (Methods section, Fig. 1a, Supplementary Fig. 1). The rotating nosepiece (turret) integrated in the commercial microscope body hold multiple standard primary objectives that work directly with the LFM module (Supplementary Fig 1), allowing different sets of imaging performance to be obtained by simple switching between different primary objectives, without replacing hardware elements in the LFM arm.

In our platform, we implemented a recent version of LFM, termed Fourier Light Field Microscopy (FLFM)[9,11,14,15], where an MLA was inserted at the Fourier plane of the detection optical light path (Fig. 1a). The MLA sub-divides the full aperture light field from the primary objective into multiple sub-aperture light fields. Each lens-let in the MLA focuses the corresponding sub-aperture light fields onto the image plane, generating multiple angular views of the 3D sample space behind each lens-let on the detection camera. This approach allows for recording, in the same 2D snapshot, both the lateral spatial information and the angular information of the light field. The original 3D sample space is recovered after image acquisition, using a deconvolution reconstruction algorithm and the experimentally measured point spread function (PSF) of the system[14,15] . Compared to the previous version of LFM where the MLA is placed at the image plane[10,13], FLFM directly forms the angular views of a 3D sample behind each lens-let in the raw LFM image, allowing for immediate inspection and analysis on the raw LFM data without 3D reconstruction. Further, FLFM does not produce grid artifact at and near the native focal plane as observed in the previous LFM version, and has improved uniformity in lateral resolution across the DOV[11,14]. Importantly, the PSF of FLFM has lateral shift invariance, and thus the deconvolution operator in the 3D reconstruction can be performed in a parallelized fashion with GPU (Graphics Processing Unit)-accelerated Fast Fourier Transform (FFT), offering approximately 100 times faster reconstruction speed compared to the previous version of LFM[14].

To design the hardware of the LFM module, we first matched the size of the MLA to the size of the camera chip so that all the angular views formed behind the MLA can be captured onto the camera, without needing an extra optical relay, and thus maintaining design simplicity. Since we used a common scientific Complementary Metal–Oxide–Semiconductor (sCMOS) camera from Hamamatsu (ORCA-Flash4.0) with chip size of 13 × 13 mm^2, we chose a commercially-available square-shaped MLA with side length of 12 mm.

We then considered two main design parameters: the focal length of lens L2 and the number of lens-lets in the MLA (Fig. 1a). The focal length of L2, denoted here as f2, was chosen to be the same with the focal length of the tube lens in the WFM (L1). This formed a 1:1 relay ratio from the back aperture of the primary objective, i.e. the Fourier plane, to the back focal plane of L2 where the MLA was placed. With the simple 1:1 relay ration, the size of the optical aperture at the MLA is the same as the size of the objective back aperture. The chosen size of the MLA, 12 x 12 mm^2, was found to be large enough to fully capture the back aperture sizes of the standard objectives used in our setup (Table 1, Supplementary Note 1). Next, we consider the number of lens-lets in the MLA, which dictates the fundamental trade-off of the light field system: 3D imaging volume vs voxel resolution. For a square MLA, the number of lens-lets can be represented using the linear dimension N defined as the number of lens-lets on one side of the square MLA (Fig. 1a). From Supplementary Table 1 (and expanded in Supplementary Note 1), we observe that increasing N leads to decreased Field of View (FOV) but increased DOV, as well as improved lateral and axial resolution. On the other hand, decreasing N results in increased FOV but decreased DOV, and degraded lateral and axial resolution. These imaging performance parameters are changing in a competing fashion with respect to N. To optimize the trade-off, we evaluated how N affects two critical imaging performance metrics for 3D imaging: the size of the resolvable reconstructed single voxel, and the number of such resolvable voxels within the captured volume (defined as the product of the lateral FOV and the axial DOV). The equations to compute these two metrics were shown in Supplementary Note 1. Both metrics achieve optimality at N ~ 9, where the number of resolvable voxels reaches maximum and the single-voxel size reaches minimum, for all of the standard primary microscope objectives (Figure 1b, c). Considering off-the-shelf commercial availability, we chose an 8 × 8 square MLA for our system. The design of other parameters in the LFM module is detailed in Supplementary Note 1. Altogether, with our design choices, and using only commercially available components, results in a LFM imaging platform that could provide optimal 3D imaging across a wide range of scales, from microns to sub-millimeters, covering cellular, tissue-levels, as well as large-scale system-level imaging (Table 1).

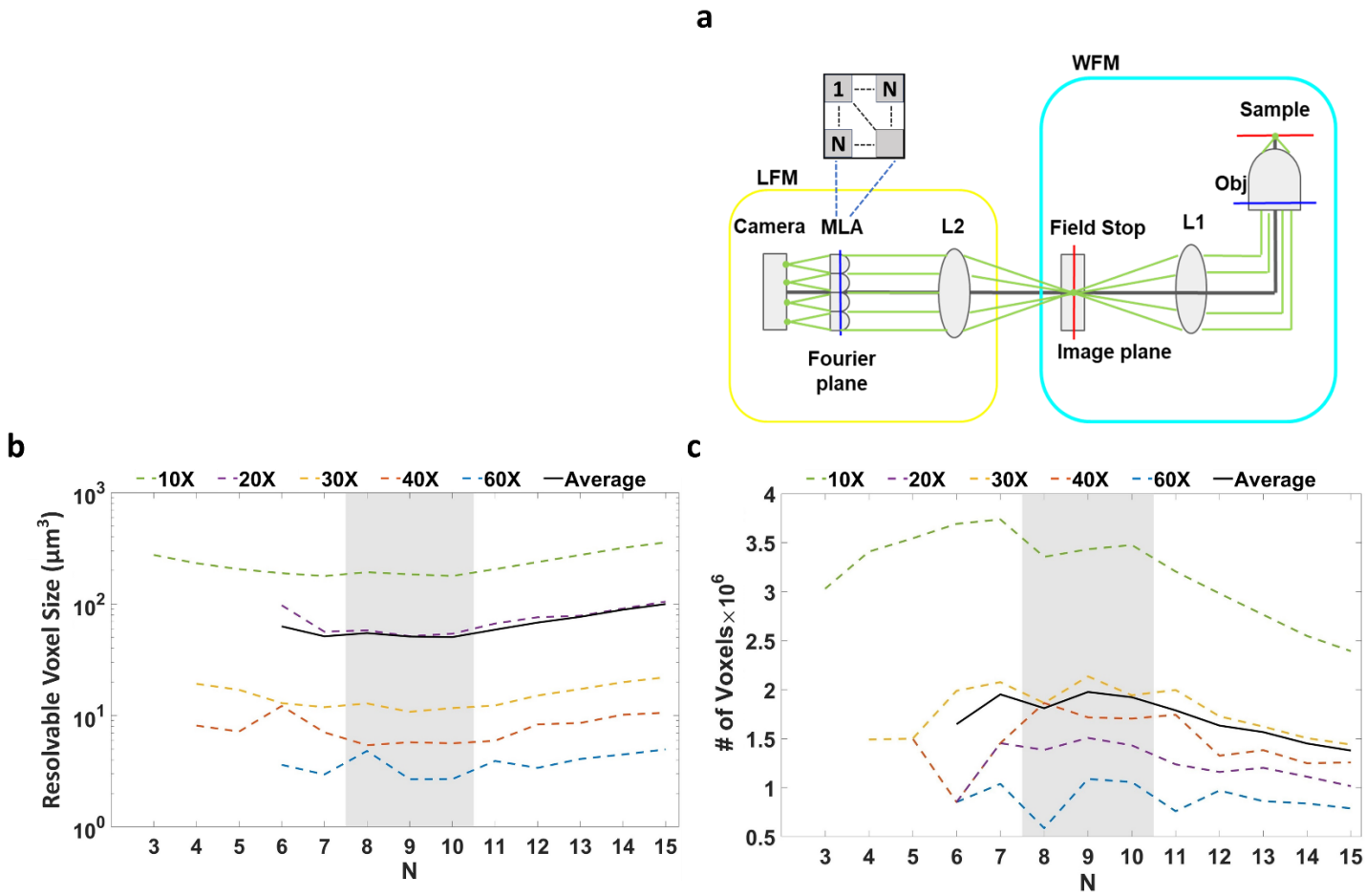

Fig. 1 Overview of the versatile FLFM system. a Field stop was appended at the image plane of the WFM body (Cyan), which is at the image plane of the optical system. The LFM module (Yellow) was consist of a relay lens L2, an MLA and a camera (Methods section). L2 propagates the back aperture (blue line) of the primary objective onto the MLA with a 1:1 ratio. The MLA was placed at the back focal plane of L2, and the raw FLFM image would form and be recorded at the back focal plane of the lens-lets on the camera. Optical Flow of the system are shown in green. Given a point source at the native object plane of WFM, the directional light ray bundle is resampled at MLA into multiple sub-aperture ray bundles and focused into multiple focal points behind each lens-let, representing multiple angular views of the light source. Insert, schematic for a N × N square MLA. N is defined as the linear dimension of a square MLA. **b,c** Single resolvable voxel size and number of resolvable voxels were plotted against N respectively, for all objectives of interest, ranging from 10X 0.4 NA Air to 60X 1.35NA Oil (Table 1). Average over all the curves were plotted in black. Grey, region of optimum N and performance. The optimum N was reached at N = ~ 9, which was the plateau area in both **b** and **c**.

Objectives						
	Magnification	60	40	30	20	10
	Numerical Aperture	1.35	1.25	1.05	0.50	0.40
	Immersion Medium	Oil	Silicone Oil	Silicone Oil	Water	Air
	Refractive Index	1.51	1.41	1.41	1.33	1.00
Depth of View (μm)		21	48	87	200	780
Field of View (diameter) (μm)		140	220	290	430	860
Lateral Resolution (μm)		1.3	2.0	2.6	4.0	8.0
Axial Resolution (μm)		2.6	3.7	5.3	14	30
Imaging Scenarios		**Cell**	**Tissue & Organoid**		**System**	

Table 1 Estimated Theoretical Imaging Performance of the versatile FLFM system. Top red chart, all the objectives of interest for different bio-imaging applications. Bottom gray chart, the corresponding imaging performance for LFM module using each primary objective. The description of theoretical performance estimation was detailed in Supplementary Note 1. As can be observed, the lower the magnification and NA of the objective, the higher the Depth of View (DOV) and the lower the resolution. The fundamental trade-off for a WFM system still holds for the FLFM system.

B. 3D reconstruction pipeline with experimentally measured point spread function (PSF)

Richardson-Lucy (RL) deconvolution was used in our pipeline for LFM 3D reconstruction[24,25]. The algorithm uses the PSF of the system and the raw LFM image to iteratively update voxel values in the 3D sample space. We obtained the PSF experimentally by imaging a sub-resolution-limit bead the over the entire DOV. In contrast to a theoretical PSF, the experimental PSF captures the hardware imperfections deviating from the theoretical design, and thus enhances the accuracy of the 3D reconstruction[23]. For each axial plane, the PSF profile is shift invariant and the bead only needs to be imaged once at the center position[14].

A unique feature of FLFM is that, in each angular view, the centroid of the PSF changes between different axial planes, encoding both lateral and axial information in a one image. This is demonstrated in the Maximum-Intensity Projection (MIP) of the PSF with the axial position coded in different colors (Fig. 2a, b). In each angular view, different colors are distributed along a tilted line instead of overlapping over each other into a spot, as is observed for a conventional 2D imaging system, e.g. WFM. Due to the uniqueness of the FLFM PSF, none of the existing PSF extraction packages can be directly applied to the FLFM bead-imaging data. To extract the PSF from the raw bead image stack, we developed a PSF processing pipeline that tracks the centroid of the PSF in each axial plane, ensuring an accurate and efficient cut-out of the PSF region (Supplementary Note 2). We offer an end-to-end pipeline from the PSF extraction to the 3D reconstruction using RL deconvolution in an open-source software package (Supplementary Software). Additional processing was conducted in Fiji [26] with a comprehensive user manual accessible to researchers without expert knowledge in LFM.

Supplementary Table 3 listed the reconstruction times for all the datasets shown in section D, E, F. Supplementary Note 2 discussed possible ways to speed up the 3D reconstruction process. Briefly speaking, the reconstruction speed can be increased by boosting the GPU processing power, utilizing cloud computing services, or down sampling the light field image data size.

C. Resolution characterization

The resolution of the LFM system is characterized by measuring the Full Width Half Maximum (FWHM) of the reconstructed single-bead images in both lateral and axial dimensions (Supplementary Fig. 2). Since the PSF is acquired from imaging a sub resolution-limit single bead, each slice of the 3D PSF is equivalent to a LFM image of a single bead positioned at a different axial depth. Therefore, to reconstruct a single bead at different axial plane, we simply need to reconstruct five slices of PSF, below and above the native focal plane, using the full 3D PSF stack. We evaluated the resolution of the LFM module with a 60x, 30x and 10x objective and reconstructed five single-bead images for each objective. For all three objectives, the FWHM measurements in both lateral and axial dimension closely matching the theoretical estimated lateral and axial resolution in Table 2 (Fig. 2c, Supplementary Fig.2). Notably, the lateral FWHM showed ~ 30% improvement over the theoretically estimated lateral resolution (Fig. 2d). This is in fact not unexpected, as deconvolution has been shown to provide better lateral resolution performance than theoretical estimates based on wave-optics approximations[23]. Overall, we achieved imaging resolutions suitable for three different biological scenarios, scaling from low resolution large volumetric system biology to high resolution subcellular environment. The scenarios are demonstrated in the following sections using zebrafish whole brain neural system activities, pancreatic beta cell calcium dynamics in mice islet and protein dynamics in cultured cells.

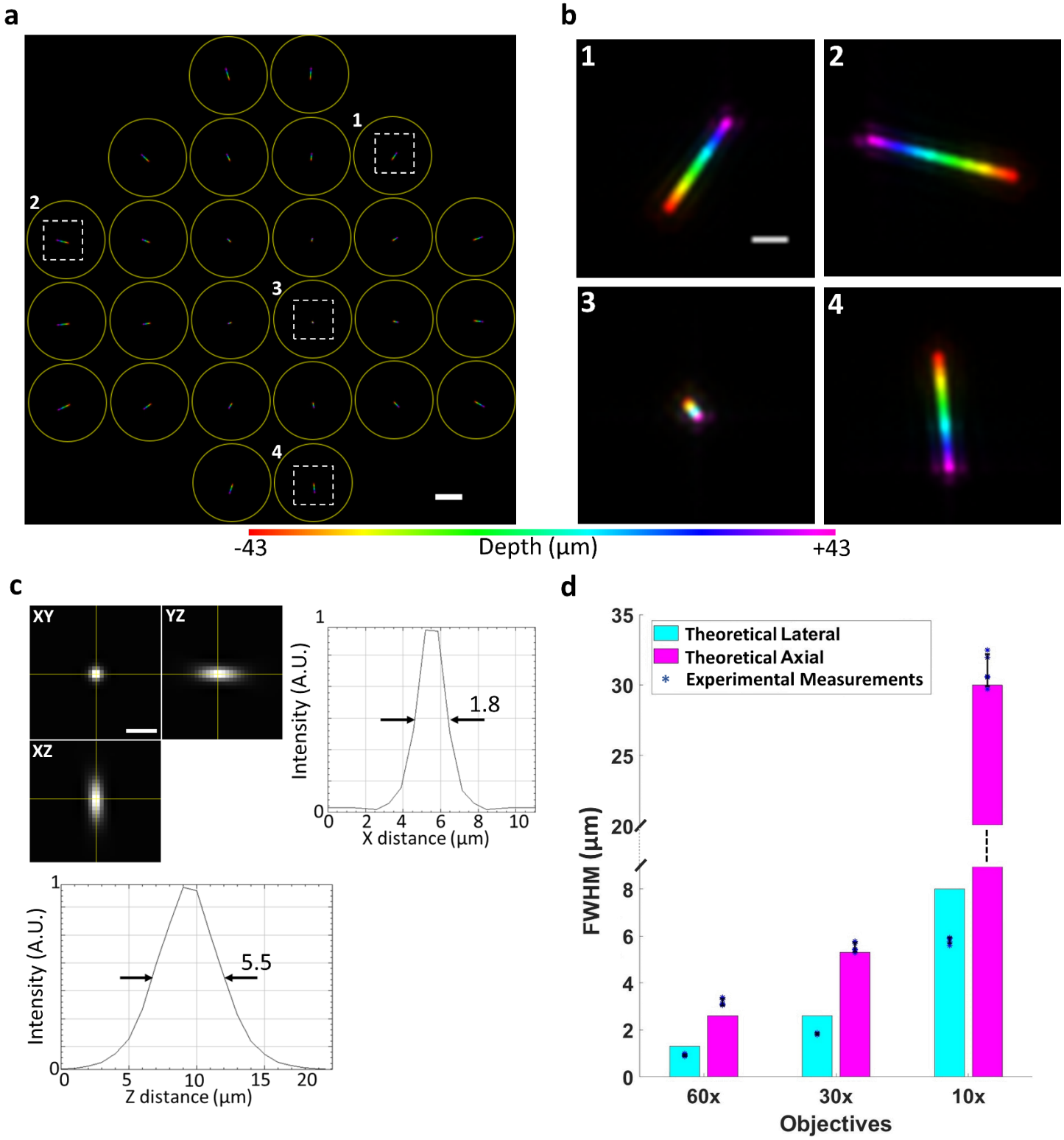

Fig. 2 Resolution characterization with beads measurement. a Maximum-Intensity Projection (MIP) of the PSF taken with 30x 1.05NA Silicone Oil immersion objective, color-coded for z-depth over the DOV from -43 µm to 43 µm. The angular views behind each lens-let are circled out in yellow. While the lens-lets are square-shaped, the field stop, determining the boundary of the FOV, is circular. **b** Zoomed in white boxes in **a**. Different angular views encodes z-depth at different lateral location. Compared to the center view (box 3), the outer angular views (box 1, 2, 4) has a more spread-out profile for the depth presentation, providing finer description in axial dimension. **c** Lateral and Axial profiles of a reconstructed bead. Orthographic slices (in XZ and YZ) show the bead profile long Z. Full Width Half Maximum (FWHM) measurements in X and Z dimensions showed lateral and axial resolution of 1.8 µm and 5.5 µm, respectively. A.U., Arbitrary Unit. **d** FWHM measurements compared to theoretical estimates of the resolutions. FWHM of five reconstructed beads were measured

for 60x, 30x and 10x and plotted in * with error bar showing the average and the standard deviation (Supplementary Table 2). Theoretical estimation of the lateral and axial resolution of three objectives (Table 1) is presented in cyan and magenta bars. On an average, both lateral and axial FWHM stay close to the theoretical estimates with the lateral FWHM exhibits a ~30% improvement. Scale bars, (**a**) 100 µm, (**b**) 10 µm, (**c**) 5 µm.

D. Imaging of seizure in zebrafish whole brain

With a low magnification primary objective, our LFM system enables capture of how fast dynamical activities develop over a large volume (~ 800 × 800 × 750 µm ^{3}um). This capability is demonstrated by imaging seizure events in zebrafish whole brain. Seizure is a large-scale whole brain neural population activity that unfolds within few seconds. Capturing the seizure events in the zebrafish whole brain requires both fast imaging speed as well as a large imaging volume. Using a 10x objective, we imaged the whole brain area of 400 × 800 × 250 µm ^{3} at 30 volumes per second (Supplementary video 1), significantly faster than the state-of-the-art seizure imaging achieved by LSM typically operated at ~5 volumes per second[27]. Even though seizure events in zebrafish model generally lasts a few seconds to minutes[28,29], the high volumetric imaging speed can sample the dynamical change at a finer time scale. By direct inspection of one lens-let image, we could identify the existence and precise timing of the seizure event, which is an important capability to facilitate trouble shooting and efficient analysis of the large datasets. In this experiment, we reconstructed a 14-second movie for one representative seizure event (Fig. 3a, b). The averaged intensity over the reconstructed whole brain region provides a coarse description of the seizure profile (Fig. 3c). To highlight the propagation sequence of the brain area, we performed a temporal difference analysis on the 3D reconstructed movie (Method). The temporal difference was computed from subtracting the previous time point intensity from the current time point intensity for each reconstructed voxel and setting the negative intensity to zero. From the temporal difference movie, we were able to observe more clearly the seizure event, from initiation to propagation throughout the whole brain (Fig. 3d, Supplementary video 1). The achieved LFM resolution (Table 1) was sufficient to discern the seizure activation and propagation across the various brain regions. We surmise that the low-resolution but high volume-coverage and high-speed LFM described here could be effectively combined with other high-resolution imaging modalities, such as LSM or confocal microscopy, where LFM provides the targeted regions of interests for the latter modalities to focus the investigations on.

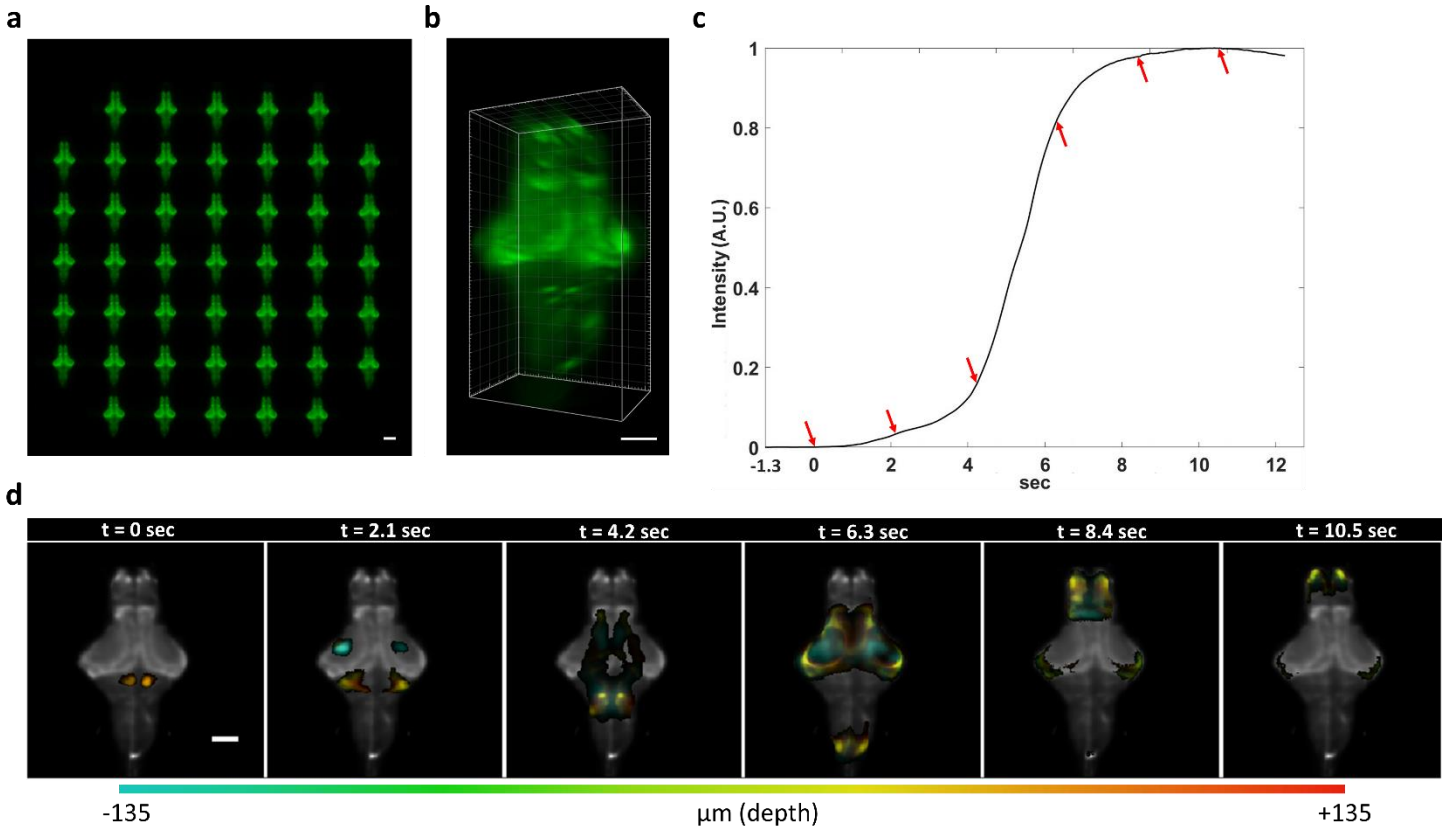

Fig. 3 Imaging seizure in zebrafish whole brain with FLFM. The fish, expressing a pan neuronal GCamp7f calcium indicator (HuC::GCaMP7f), was immobolized in agarose and the seizure was chemically induced by administering 15mM PTZ (Method). The imaging is performed using 10x 0.4NA oil immersion as the primary objective. The calcium activity was recorded at 30 volumes/s over a volume size of ~860 × 860 × 270 μm^3. **a** One timeframe of FLFM recording shows different angular views of the fish brain. **b** 3D Reconstruction of **a** rendered in 3D. The reconstructed volume has 27 z slices with each z slice of 10 µm. The rendering shows the active neurons located in different areas of the brain. **c** Averaged intensity in the brain region traced over time during one seizure event. Red arrows, time points at 2.1 sec apart with the first arrow pointing at the seizure. A.U., Arbitrary Unit. **d** Depth color-coded temporal difference intensity (Method) at the time points in **c**. The seizure initialized (t = 0 sec) in the cerebellum area of the fish brain, spread out along both rostral and caudal directions. Gray scale, the average intensity over time and over axial direction presented as a contrast for the dynamical intensity. Scale bars, a 100 µm, b 100 µm, d 100 µm.

E. Imaging calcium dynamic in mice islet

Calcium dynamics in pancreatic beta cells are fundamental for sensing glucose levels and secreting insulin appropriately, playing a vital role in maintaining glucose homeostasis and overall metabolic health[30–32]. Beta cell calcium dynamics within mouse islets have been commonly imaged with conventional microscopy such as confocal microscope, WFM, or LSM[33–39]. While these conventional imaging modalities can achieve high imaging speed for single 2D plane, imaging calcium dynamics in the entire 3D islet structure remains a challenge. Currently, state-of-the-art 3D imaging speed for whole mice islets operates at ~1 second per volume[35]. Given that the intrinsic cellular dynamic happens at sub-second time scale[40,41], the speed for capturing dynamics in 3D is low, resulting in an under-sampling of the true signals and potentially leading to omission of crucial information. While these conventional imaging modalities can achieve relatively adequate speed for imaging single 2D planes, capturing calcium dynamics in the entire 3D islet structure remains a challenge. Often, compromises in axial coverage and/or sampling must be made, leading to potential under-sampling of the true spatial-temporal signals.

The 3D snap-shot feature of the LFM provides a solution for this challenge. Using the 30x objective, we imaged the beta cells labeled with GCamp6f at 20 volumes per second in a whole mice islet immersed in constant glucose medium (Method). The high volumetric frame rate allows for tracking fast calcium dynamics traveling in 3D across the entire islet. To showcase the dynamics, we recorded and reconstructed a 70-second movie of the calcium dynamics in the entire islet (Fig. 2a, b, Supplementary movie 2). From the spatial average intensity traces over time (Method), repetitive calcium activation events were observed within the islet (Fig. 2c). However, 3D imaging empowered with our LFM revealed diverse calcium activation propagation patterns changing at sub-second scale across the 3D space. This characteristic is demonstrated by the temporal difference movie of the 3D reconstruction (Method, Supplementary movie 2) and highlighted using the temporal difference of three separate events with color-coded z depth (Fig. 2d). As shown in Fig. 2d, different events initiated at different 3D locations (at t = 0 sec) and propagated through the islet in different patterns.

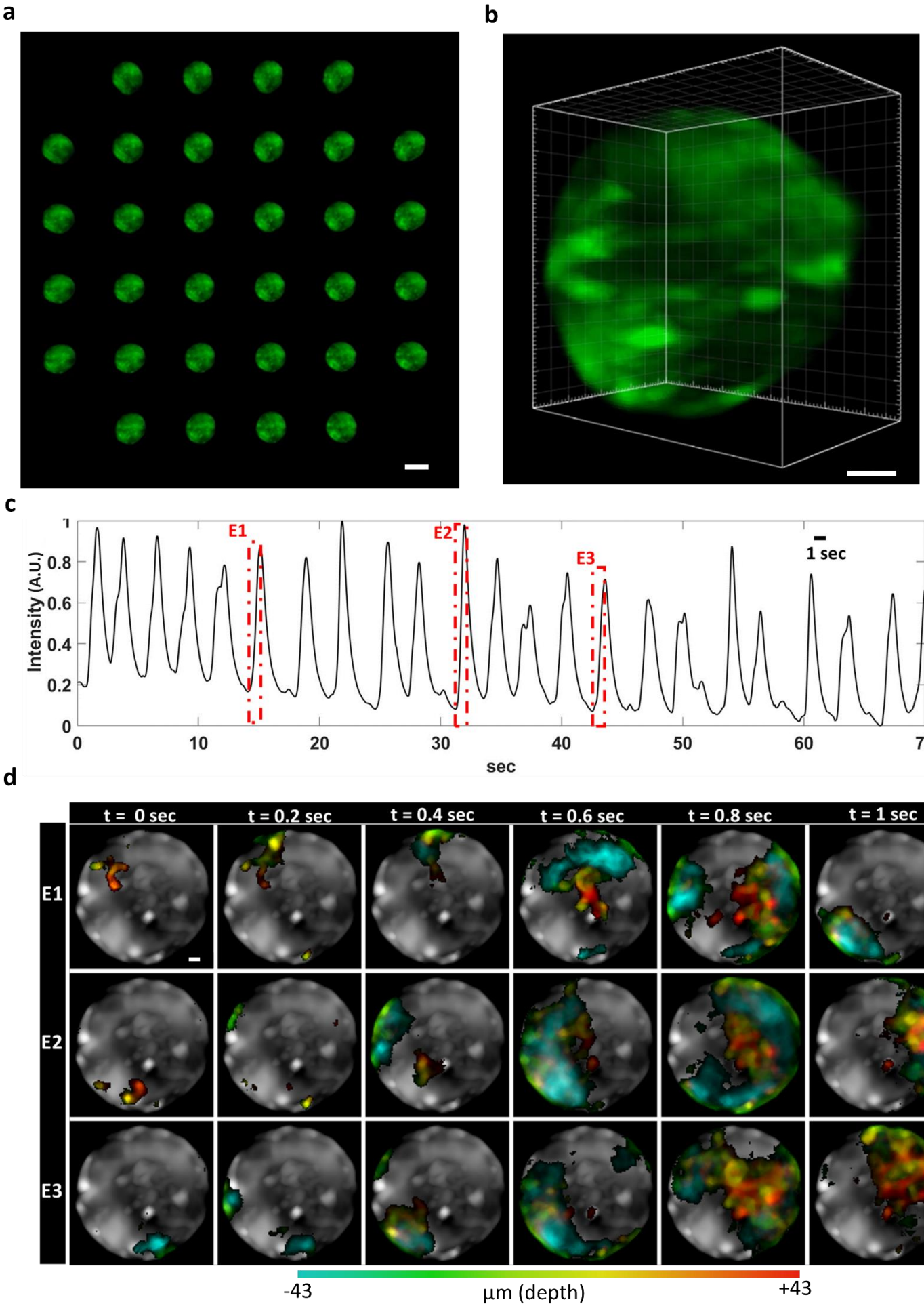
a
b
c
E1
E2
E3
1 sec
Intensity (A.U.)
0
0.2
0.4
0.6
0.8
1
0
10
20
30
40
50
60
70
sec
d
t = 0 sec
t = 0.2 sec
t = 0.4 sec
t = 0.6 sec
t = 0.8 sec
t = 1 sec
E1
E2
E3
-43
µm (depth)
+43

Fig. 4 Calcium imaging in whole a mouse islet with FLFM. Functional imaging of a mice islet with calcium indicator GCaMP6f expressed in pancreatic beta cells. The islet was rest in the medium glucose concentration (~11mM) for ~5 days prior to imaging. The imaging is performed using 30x silicone oil immersion as the primary objective. The calcium activity was recorded at 20 volumes/s over a volume size of ~100 × 100 × 86 μm^3. **a** One timeframe of FLFM recording shows different angular views of the islet. **b** 3D Reconstruction of **a** rendered in 3D. The reconstructed volume has 43 z slices with each z slice of 2 µm. The rendering shows the calcium activities in the islet at different spatial locations in 3D. **c** Averaged intensity in the islet region traced over 70 s. Red dotted boxes, the rising edge of three calcium events (E1, E2, E3). A.U., Arbitrary Unit. **d** Depth color-coded temporal difference intensity (Method) at six time points for E1, E2, E3 in **c**. Comparing vertically and horizontally, each event initiated at different 3D location (t = 0 sec) and propagated through the islet in different patterns. Gray scale, the average intensity over time and over axial direction presented as a contrast for the dynamical intensity. Scale bars, **a** 100 µm, **b** 20 µm, **d** 10 µm.

F. Imaging protein dynamics in cultured cells

Toward the smaller scale, our LFM can achieve high resolution bio-imaging by using a primary objective with high magnification and high Numerical Aperture (NA). Under this setting, 3D dynamics at subcellular level can be captured with high volumetric frame rate. To demonstrate this, we imaged protein dynamics in cultured cells with a 60x objective (Method), achieving lateral and axial resolution of 0.9 µm and 3.2 µm (Supplementary Table 2). The cell we imaged was a Human Bone Osteosarcoma Epithelial Cell (U2OS line) expressing mNeonGreen fused to the human prolactin receptor (Method). The human prolactin receptor (hPRLR) plays a crucial role in various physiological processes and diseases including breast cancer, autoimmune disease and metabolic disorders [...]. Understanding hPRLR is essential for advancing knowledge in these areas and improving related therapies.

In the experiment, we captured the rapid movement of the protein across 17 µm of z-depth (Fig. 5a, b, Supplementary video 3), presenting a promising way for investigating protein trafficking and interactions in the singe cell. Even with the reduced resolution of LFM, we could still visualize the dynamics between the protein clusters distributed throughout the entire cell (Fig. 5c, d, e, f). This observed resolution could be further enhanced by using a higher magnification objective. In addition, LFM has the advantage of hardware simplicity at a low cost and can be easily integrated with other commercial imaging systems, serving as a convenient way to probe subcellular dynamical processes.

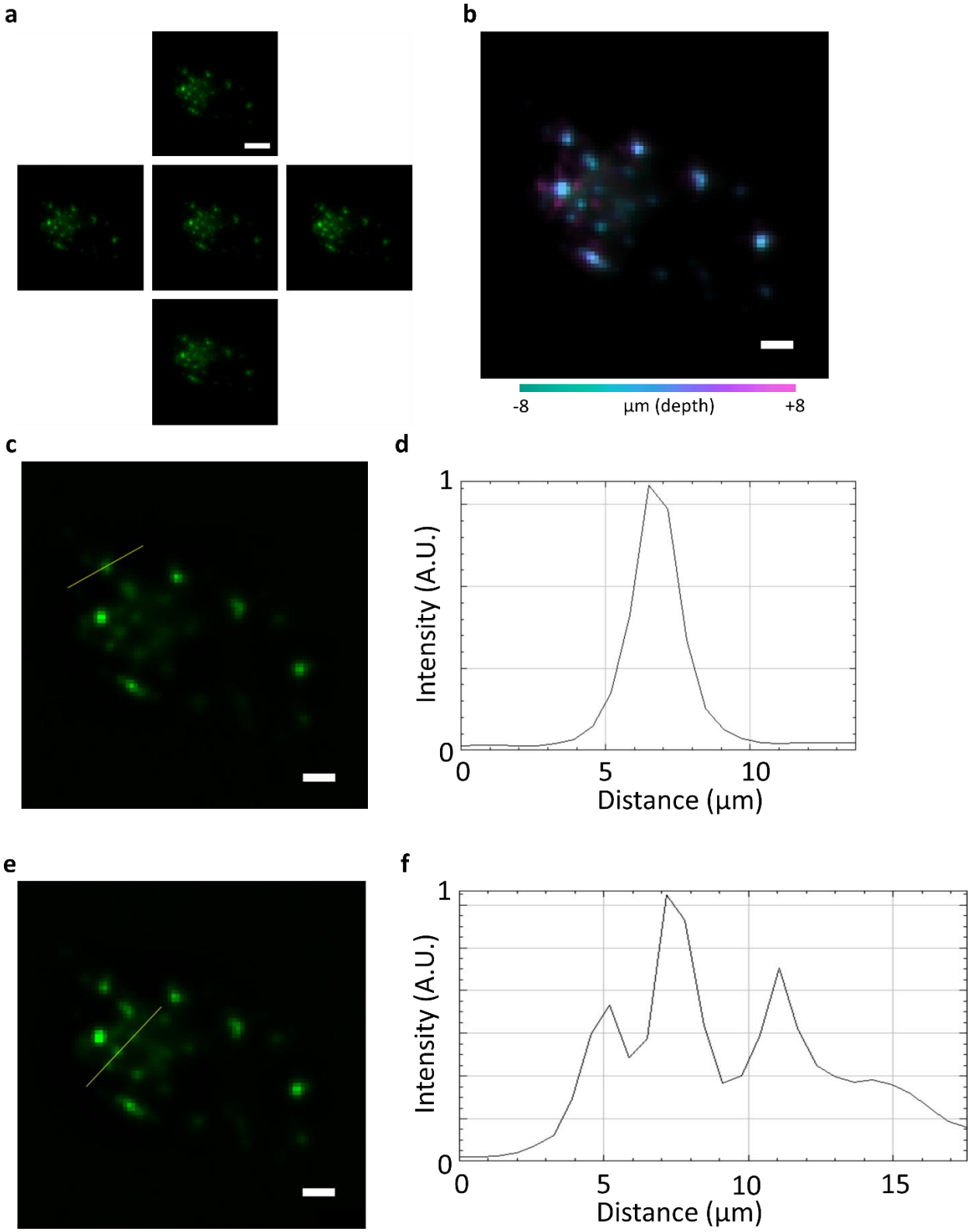

Fig. 5 Imaging protein dynamics in cultured cells with FLFM. The cell is Human Bone Osteosarcoma Epithelial Cell (U2OS line) expressing mNeonGreen fused to the human prolactin receptor (Method). The imaging is performed using 60x 1.35NA oil immersion as the primary objective. The dynamics was recorded at 20 volumes/s over a volume size of ~144 × 144 × 21 μm^3 (Supplementary video 3). **a** One timeframe of FLFM recording shows different angular views of the cultured cell. **b** 3D Reconstruction of **a** with color coded z depth. The reconstructed volume has 17 z slices with each z slice at 1 µm step. The image shows the 3D distribution of the protein at one time point. **c, e** z slices at -1 µm and 1 µm, respectively, in the reconstructed volume in **b**. **d, f** Line profile of the yellow line in **c** and **e**. A.U., Arbitrary Unit. Scale bars, 5 µm.

III. CONCLUSIONS

The results of this research present an improved LFM implementation easily accessible to researchers in a wide range of biology disciplines. By integrating the LFM with a commercial wide field microscope body, we demonstrate the improved versatility of our LFM system, observing various 3D dynamical process ranging from sub-cellular protein dynamics to cellular calcium signaling to the zebrafish whole brain neural network. In addition, the built-in flexibility and ease of use of the commercial microscope body makes the LFM module accessible and user-friendly. Instead of a wide field microscope, LFM can also be integrated in a similar manner with other 2D imaging systems, such as a confocal microscope or LSM, serving as an add-on module for rapid 3D dynamical capture. In particular, the integration with LSM enables selective volume illumination (SVIM)[42,43], which has been shown to improve contrast and resolution over wide field illumination. The resolution and imaging volume of the versatile LFM platform could be further optimized with a customized MLA[23], as well as larger camera sensor size that allows for either more angular views to be captured or higher pixel sampling rate. Further magnification or de-magnification could be done between the MLA and camera to make full use of the camera chip size, realizing the true optical resolution limit. To further enhance the accessibility of the system, an all-in-one Graphical user interface (GUI), streamlining the process from hardware design to 3D reconstruction, would facilitate users less experienced in optics and computational imaging to independently design their own system and handle the raw LFM data. As computing power continues to advance, our versatile LFM platform has the potential to reach more researchers and provides imaging solutions to a broad range of biological applications, empowering scientists to explore more interesting biological questions and unlock new working principles of life science.

Reference:

1. Schneckenburger, H. & Richter, V. Challenges in 3D Live Cell Imaging. *Photonics* **8**, 275 (2021).
2. Muldoon, S. F. & Bassett, D. S. Network and Multilayer Network Approaches to Understanding Human Brain Dynamics. *Philos. Sci.* **83**, 710–720 (2016).
3. Palm, G. Neural Information Processing in Cognition: We Start to Understand the Orchestra, but Where is the Conductor? *Front. Comput. Neurosci.* **10**, 3–3 (2016).
4. Saleem, S. & Kannan, R. R. Zebrafish: an emerging real-time model system to study Alzheimer's disease and neurospecific drug discovery. *Cell Death Discov.* **4**, 45–45 (2018).
5. Morgan, V. L., Abou-Khalil, B. & Rogers, B. P. Evolution of functional connectivity of brain networks and their dynamic interaction in temporal lobe epilepsy. *Brain Connect.* **5**, 35–44 (2015).
6. Zhang, Z. *et al.* Dynamic functional connectivity and its anatomical substrate reveal treatment outcome in first-episode drug-naïve schizophrenia. *Transl. Psychiatry* **11**, 282–282 (2021).
7. Elliott, A. D. Confocal Microscopy: Principles and Modern Practices. *Curr. Protoc. Cytom.* **92**, e68–e68 (2020).
8. Stelzer, E. H. K. *et al.* Light sheet fluorescence microscopy. *Nat. Rev. Methods Primer* **1**, (2021).
9. Scrofani, G. *et al.* FIMic: design for ultimate 3D-integral microscopy of in-vivo biological samples. *Biomed. Opt. Express* **9**, 335–346 (2017).
10. Levoy, M., Ng, R., Adams, A., Footer, M. & Horowitz, M. Light field microscopy. *ACM Trans. Graph.* **25**, 924–934 (2006).
11. Llavador, A., Sola-Pikabea, J., Saavedra, G., Javidi, B. & Martínez-Corral, M. Resolution improvements in integral microscopy with Fourier plane recording. *Opt. Express* **24**, 20792 (2016).
12. Kim, K. Single-Shot Light-Field Microscopy: An Emerging Tool for 3D Biomedical Imaging. *BioChip J.* **16**, 397–408 (2022).
13. Broxton, M. *et al.* Wave optics theory and 3-D deconvolution for the light field microscope. *Opt. Express* **21**, 25418–25439 (2013).
14. Guo, C., Liu, W., Hua, X., Li, H. & Jia, S. Fourier light-field microscopy. *Opt. Express* **27**, 25573–25594 (2019).
15. Galdón, L., Saavedra, G., Garcia-Sucerquia, J., Martínez-Corral, M. & Sánchez-Ortiga, E. Fourier lightfield microscopy: a practical design guide. *Appl. Opt.* **61**, 2558 (2022).

16. Pégard, N. C. *et al.* Compressive light-field microscopy for 3D neural activity recording. *Optica* **3**, 517 (2016).

17. Yoon, Y.-G. *et al.* Sparse decomposition light-field microscopy for high speed imaging of neuronal activity. *Optica* **7**, 1457 (2020).

18. Zhang, Z., Cong, L., Bai, L. & Wang, K. Light-field microscopy for fast volumetric brain imaging. *J. Neurosci. Methods* **352**, 109083 (2021).

19. Sims, R. R. *et al.* Single Molecule Light Field Microscopy. (2020) doi:10.1101/2020.05.20.104802.

20. Guo, C., Li, H. & Jia, S. Fast, volumetric live-cell imaging using high-resolution light-field microscopy. in (OSA, 2019). doi:10.1364/ntm.2019.ns1b.1.

21. Shaw, M. *et al.* Three-dimensional behavioural phenotyping of freely moving C. elegans using quantitative light field microscopy. *PloS One* **13**, e0200108–e0200108 (2018).

22. Prevedel, R. *et al.* Simultaneous whole-animal 3D imaging of neuronal activity using light-field microscopy. *Nat. Methods* **11**, 727–730 (2014).

23. Cong, L. *et al.* Rapid whole brain imaging of neural activity in freely behaving larval zebrafish (Danio rerio). *eLife* **6**, e28158 (2017).

24. Lucy, L. B. An iterative technique for the rectification of observed distributions. *Astron. J.* **79**, 745 (1974).

25. Richardson, W. H. Bayesian-Based Iterative Method of Image Restoration*. *J. Opt. Soc. Am.* **62**, 55 (1972).

26. Schindelin, J. *et al.* Fiji: an open-source platform for biological-image analysis. *Nat. Methods* **9**, 676–682 (2012).

27. de Vito, G. *et al.* Fast whole-brain imaging of seizures in zebrafish larvae by two-photon light-sheet microscopy. *Biomed. Opt. Express* **13**, 1516–1536 (2022).

28. Cho, S.-J. *et al.* Zebrafish as an animal model in epilepsy studies with multichannel EEG recordings. *Sci. Rep.* **7**, 3099–3099 (2017).

29. Gawel, K. *et al.* Seizing the moment: Zebrafish epilepsy models. *Neurosci. Biobehav. Rev.* **116**, 1–20 (2020).

30. Klec, C., Ziomek, G., Pichler, M., Malli, R. & Graier, W. F. Calcium Signaling in ß-cell Physiology and Pathology: A Revisit. *Int. J. Mol. Sci.* **20**, 6110 (2019).

31. Rorsman, P. & Ashcroft, F. M. Pancreatic β-Cell Electrical Activity and Insulin Secretion: Of Mice and Men. *Physiol. Rev.* **98**, 117–214 (2018).

32. Podobnik, B. *et al.* β Cells Operate Collectively to Help Maintain Glucose Homeostasis. *Biophys. J.* **118**, 2588–2595 (2020).

33. Zmazek, J. *et al.* Assessing Different Temporal Scales of Calcium Dynamics in Networks of Beta Cell Populations. *Front. Physiol.* **12**, 612233–612233 (2021).

34. Kravets, V. *et al.* Functional architecture of pancreatic islets identifies a population of first responder cells that drive the first-phase calcium response. *PLoS Biol.* **20**, e3001761–e3001761 (2022).

35. Zhao, J. *et al.* In vivo Imaging of Calcium Activities from Pancreatic β-cells in Zebrafish Embryos Using Spinning-disc Confocal and Two-photon Light-sheet Microscopy. *Bio-Protoc.* **11**, e4245–e4245 (2021).

36. Zhao, J. *et al.* In vivo imaging of β-cell function reveals glucose-mediated heterogeneity of β-cell functional development. *eLife* **8**, e41540 (2019).

37. Akalestou, E. *et al.* Intravital imaging of islet Ca(2+) dynamics reveals enhanced β cell connectivity after bariatric surgery in mice. *Nat. Commun.* **12**, 5165–5165 (2021).

38. Lavagnino, Z. *et al.* Snapshot Hyperspectral Light-Sheet Imaging of Signal Transduction in Live Pancreatic Islets. *Biophys. J.* **111**, 409–417 (2016).

39. Kenty, J. H. R. & Melton, D. A. Testing pancreatic islet function at the single cell level by calcium influx with associated marker expression. *PloS One* **10**, e0122044–e0122044 (2015).

40. Zhang, Y. *et al.* Fast and sensitive GCaMP calcium indicators for imaging neural populations. *Nature* **615**, 884–891 (2023).

41. Chen, T.-W. *et al.* Ultrasensitive fluorescent proteins for imaging neuronal activity. *Nature* **499**, 295–300 (2013).

42. Truong, T. V. *et al.* High-contrast, synchronous volumetric imaging with selective volume illumination microscopy. *Commun. Biol.* **3**, 74–74 (2020).

43. Keomanee-Dizon, K., Fraser, S. E. & Truong, T. V. A versatile, multi-laser twin-microscope system for light-sheet imaging. *Rev. Sci. Instrum.* **91**, 053703–053703 (2020).

44. Edelstein, A. D. *et al.* Advanced methods of microscope control using μManager software. *J. Biol. Methods* **1**, e10 (2014).

45. Zhong, L. *et al.* Essential role of Skp2-mediated p27 degradation in growth and adaptive expansion of pancreatic beta cells. *J. Clin. Invest.* **117**, 2869–2876 (2007).

Method

Hardware setup. The optical setup was composed of two subsystems: the commercial WFM (Olympus, IX83 Inverted Microscope) and the customized LFM (Supplementary Fig. 1). The WFM is equipped with a fluorescence light source (Olympus, U-HGLGPS) and standard filter cube sets for different colors. The customized LFM module was appended to the left camera port of the WFM body. In the LFM module, a field stop was placed at the image plane to control of the size of the field of view so that each lens-let image does not overlap each other[1–3]. A relay lens was positioned one focal length behind the field stop. Coupled with the WFM internal tube lens, the relay lens relayed the back aperture plane (Fourier plane) of the primary objective onto the MLA. A sCmos Camera (Hamamatsu, ORCA-Flash4.0) was placed at the back focal plane of the lens-let where different angular projection views of the 3D sample were formed. For imaging in LFM mode, the light source was filtered to a desired wavelength and directed to the left camera port in the WFM system. The emission light in all three biological samples were green and filtered by a FITC filter cube set (Olympus, U-FF). Image acquisition process was controlled by Micro-Manager[4]. Final hardware set-ups are shown in Supplementary Fig. 1. The key hardware components are summarized in supplementary Table 1.

Zebrafish experiments. Zebrafish larvae with pan neuronal GCaMP7f expression have been imaged at 5 d.p.f. (days post fertilization) using the fish line HuC:GCamp7f Zebrafish. *Pentylenetetrazole (PTZ) solution composition*: PTZ was purchased from Cayman Chemicals (Item 18682) and diluted into 45 uL 1M aliquot solutions (dissolved in UltraPureTM Distilled Water from Invitrogen by Life Technologies) that remain frozen until used. *Fish preparation*: The zebrafish was mounted in an agarose solution (1800 uL of 1.5% agarose & 1155 uL of egg water of the agarose) and placed in the FLFM caddy where it can be imaged. Once ready to image, a 45uL 1M aliquot of the PTZ was added directly to the petri dish solution (the total volume of the petri dish solution to 3mL) using a pipette. The overall concentration of PTZ in the solution in the petri dish to 15 mM, which is the intended concentration for observed seizure activity. *Imaging*: The zebrafish brain was placed on the WFM stage and positioned at the center of the field of view. The focal plane was adjusted to achieve the sharpest view of the sample. The imaging exposure time was set to 33.3 ms per frame which resulted in a volumetric imaging rate of 30 HZ. The recording began exactly 1 minute after the 45 uL of 1M PTZ solution was added to the petri dish. The 1-minute delay was to account for the time needed to close the incubator surrounding the petri dish and make sure the specimen was properly placed in the imaging field of view. The dynamics were recorded for 90 minutes, and the 3D reconstruction was conducted on one event of 15 seconds.

Mice islet experiments. *Animal Model:* All animal studies were approved and completed per the CHLA Institutional Animal Care and Usage Committee. Ins1Cre-GCaMP6f, β cell-specific GCaMP6f protein expression, were generated by crossing Ins1Cre mice (The Jackson Laboratory #026801) and Ai95(RCL-GCaMP6f)-D (The Jackson Laboratory #028865) both on a C57Bl/6J background. *Islet Isolation and Dissociation:* Islets were isolated using a 3.5 mg/mL liberase and 1.5 mg/mL DNAse enzyme blend (Roche Diagnostics, *Indianapolis, IN, USA*) as previously described[5]. Briefly, the enzyme solution was perfused into the pancreas via the bile duct, and the inflated pancreas was removed for further digestion at 37 °C for 12 min. Extracted islets were hand-picked under a fluorescence light microscope to isolate Ins1Cre-GCaMP6f islets and incubated with Roswell Park Memorial Institute (RPMI) 1640 (Gibco, New York, NY, USA). Islets were transferred into an 8-well imaging chamber (Ibidi #80826) with RPMI 1640 and left at 37 °C overnight before being used for experiments. On the day of imaging, islets were either left in RPMI 1640 or equilibrated in Kreb's Ringer bicarbonate buffer as previously described[5] at 2.8mM basal glucose concentration and then increased to 16mM static glucose incubation. *Imaging*: The islet was placed on the WFM stage and positioned at the center of the field of view. The focal plane was adjusted to achieve the sharpest view of the sample. The imaging exposure time was set to 50 ms per frame which resulted in a volumetric imaging rate of 20 HZ. The dynamics were recorded for 70 seconds.

Cell experiments. *Plasmid design:* A plasmid containing human prolactin receptor (hPRLR), fused to the rat PRLR signal peptide, was obtained as a gift from Vincent Goffin (INSERM, Paris, France). pcDNA3 Flag HA (#10792) plasmid was obtained from Addgene. The rat PRLR signal peptide, hPRLR, and the fluorescent protein mNeonGreen were cloned into the pcDNA3 plasmid using Takara In-Fusion Snap Assembly (#638947) according to the manufacturer's protocol, such that

mNeonGreen was fused to the C-terminus of hPRLR. U2OS cells were acquired from the American Type Culture Collection (Manassas, VA). *Cell culture*: Cells were cultured in DMEM (Corning, #10-013-CV), supplemented with 10% fetal bovine serum (Thermo Fisher Scientific, #A5256701), 1% penicillin/streptomycin (Thermo Fisher Scientific, #15140122), and 1% L-glutamine (Sigma-Aldrich, #G7513). For imaging experiments, cells were grown to ~80% confluency before being seeded onto 8-well #1.5 glass chambered coverslips (ibidi, #80807). 24 h after seeding, transient transfection of the pcDNA3-hPRLR-mNeonGreen plasmid was performed using Lipofectamine 3000 and P3000 reagents (Thermo Fisher Scientific, #L30008) according to the manufacturer's protocol. 24 h after transfection, cell culture medium was replaced with phenol red-free Leibovitz's L-15 medium (Thermo Fisher Scientific, #21083027) for imaging. *Imaging*: The cell was placed on the WFM stage and positioned at the center of the field of view. The focal plane was adjusted to achieve the sharpest view of the sample. The imaging exposure time was set to 50 ms per frame which resulted in a volumetric imaging rate of 20 HZ. The dynamics were recorded for 50 seconds.

Richardson-Lucy (RL) deconvolution. LFM 3D reconstruction problem was solved using RL deconvolution method as described in previous literature[6–8]. Briefly speaking, if we arrange both the 2D image space and the 3D voxel space into vectors, light field imaging system can be written as a matrix vector multiplication wrapped by Poisson noise model. Let's denote $\vec{g}$ as the vectorized 3D volume, $\vec{f}$ as the vectorized raw 2D light field image, $Pois\{\cdot\}$ as the Poisson process and $\mathbf{H}$ as the PSF matrix where each column is the PSF of each voxel. The forward image formation process is characterized in equation (1):

$$\vec{f} \sim Pois\{\mathbf{H} \cdot \vec{g}\} \tag{1}$$

The PSF matrix $\mathbf{H}$ and raw light field image $\vec{f}$ from experiments were acquired from the experiments. The goal of the reconstruction is to solve the unknow vector $\vec{g}$. RL deconvolution was derived to solve this problem[9,10]. The deconvolution algorithm starts with an initial guess of $\vec{g}$, then iteratively update the entry values in $\vec{g}$ until convergence. The initiation and update are shown in equation (2) and (3). The division $\frac{\square}{\square}$ represents an element-wise division. Superscript T represents transpose operator. k denotes the iteration times.

$$Initialization: \quad k = 0, \qquad \vec{g}^0 = \mathbf{H}^T \cdot \vec{f} \tag{2}$$

$$Update: \quad k = k + 1, \quad \vec{g}^{k+1} = \vec{g}^k \cdot \mathbf{H}^T \cdot \left(\frac{\vec{f}}{\mathbf{H} \cdot \vec{g}^k}\right) \tag{3}$$

Specifically, in the update section, $\mathbf{H} \cdot \vec{g}^k$ represents the forward projection process from the estimated 3D volume to the estimated 2D light field image. The pixel-wise discrepancies between the estimated 2D light field image and the true raw light field image are calculated with the element-wise division operator $\frac{\vec{f}}{\mathbf{H} \cdot \vec{g}^k}$. The discrepancies are backward projected through $\mathbf{H}^T \cdot \left(\frac{\vec{f}}{\mathbf{H} \cdot \vec{g}^k}\right)$ to update the estimated volume. Since the PSF is shift-invariant in each axial plane, forward and backward projection can be computed with 2D convolution using Fast Fourier Transform (FFT)[6,11]. The computation is accelerated with Graphics Processing Unit (GPU). For all the reconstruction in this work, we set the total number of iterations to be 10. After 10 iterations, indiscernible differences were generally not observed in the reconstructed volume. Detailed discussion on computation time is provided in Supplementary Note 2.

3D temporal difference analysis. The temporal difference analysis is preceded by a 3D spatial filtering and voxel-wise temporal filtering sequentially. First, each reconstructed 3D frames were filtered spatially by a 3D median filter of size 5 × 5 × 5. After the spatial filtering, the signal trace of each voxel was filtered by a low-pass Butterworth filter thresholding at 3HZ. The temporal difference analysis was then applied to the filtered 3D reconstruction voxel by voxel as well. Let's denote a voxel intensity value at any time point t = i as v^i. Consider the time point starts at t = 0 and ends at t= T. The temporal difference at t = i of each voxel is defined in (1) as:

$$v_d^i = max(0, v^i - v^{i-1}), \; i \in [2, T) \tag{1}$$

where the negative intensity was set to zero. The temporal difference was computed for all the voxels within the filtered 3D reconstructed region from the second frame to the last frame. The trace of the temporal difference represents the increase in signal intensity at each time point relative to the last time point, highlighting the signal initialization and propagation over time across the 3D volume.

Method Reference:

1. Llavador, A., Sola-Pikabea, J., Saavedra, G., Javidi, B. & Martínez-Corral, M. Resolution improvements in integral microscopy with Fourier plane recording. *Optics Express* **24**, 20792 (2016).

2. Scrofani, G. *et al.* FIMic: design for ultimate 3D-integral microscopy of in-vivo biological samples. *Biomed Opt Express* **9**, 335–346 (2017).

3. Galdón, L., Saavedra, G., Garcia-Sucerquia, J., Martínez-Corral, M. & Sánchez-Ortiga, E. Fourier lightfield microscopy: a practical design guide. *Applied Optics* **61**, 2558 (2022).

4. Edelstein, A. D. *et al.* Advanced methods of microscope control using μManager software. *J Biol Methods* **1**, e10 (2014).

5. Zhong, L. *et al.* Essential role of Skp2-mediated p27 degradation in growth and adaptive expansion of pancreatic beta cells. *J Clin Invest* **117**, 2869–2876 (2007).

6. Guo, C., Liu, W., Hua, X., Li, H. & Jia, S. Fourier light-field microscopy. *Opt Express* **27**, 25573–25594 (2019).

7. Broxton, M. *et al.* Wave optics theory and 3-D deconvolution for the light field microscope. *Opt Express* **21**, 25418–25439 (2013).

8. Prevedel, R. *et al.* Simultaneous whole-animal 3D imaging of neuronal activity using light-field microscopy. *Nat Methods* **11**, 727–730 (2014).

9. Lucy, L. B. An iterative technique for the rectification of observed distributions. *The Astronomical Journal* **79**, 745 (1974).

10. Richardson, W. H. Bayesian-Based Iterative Method of Image Restoration*. *Journal of the Optical Society of America* **62**, 55 (1972).

11. Cong, L. *et al.* Rapid whole brain imaging of neural activity in freely behaving larval zebrafish (Danio rerio). *Elife* **6**, e28158 (2017).